PAPER

High-density magnetic-vacancy inclusion in Co_2MnGa single crystal probed by spin-polarized positron annihilation spectroscopy

IOP Publishing Journal of Physics: Condensed Matter
J. Phys.: Condens. Matter **34** (2022) 045701 (9pp) https://doi.org/10.1088/1361-648X/ac3304

High-density magnetic-vacancy inclusion in Co_2MnGa single crystal probed by spin-polarized positron annihilation spectroscopy

A Miyashita[1], M Maekawa[1], Y Shimoyama[1], N Seko[1], A Kawasuso[1,*] and R Y Umetsu[2]

[1] National Institutes for Quantum and Radiological Science and Technology, 1233 Watanuki, Takasaki, Gunma 370-1292, Japan
[2] Institute for Materials Research, Tohoku University, 2-1-1 Katahira, Sendai, Miyagi 980-8577, Japan

E-mail: kawasuso.atsuo@qst.go.jp

Received 29 June 2021, revised 29 September 2021
Accepted for publication 25 October 2021
Published 9 November 2021

Abstract

Co_2MnGa is a Weyl semimetal exhibiting giant anomalous Hall and Nernst effects. Using spin-polarized positron annihilation spectroscopy, we examined a Bridgman-grown Co_2MnGa single crystal with a nearly perfect $L2_1$-ordered structure and a reference Co_2MnAl polycrystal with a Mn–Al-disordered $B2$ structure. We found that a large amount of magnetic vacancies (more than 100 ppm) were included in the Co_2MnGa crystal but not the Co_2MnAl crystal. We discuss possible reasons for the inclusion of vacancies, the role of vacancies in the development of the ordered structure, and the electronic states associated with the vacancies. Toward the development of Co_2MnGa-based devices, the manners for reducing vacancies as well as the influence of vacancies on the electrical transport properties should be considered.

Keywords: Co_2MnGa, Weyl semimetal, positron annihilation spectroscopy, spin, vacancy, electronic states

(Some figures may appear in colour only in the online journal)

1. Introduction

In 2016, Co_2MnGa and Co_2MnAl, which are two kinds of full Heusler alloys, were theoretically predicted to be ferromagnetic Weyl semimetals with potential applications in spintronic devices [1]. The Weyl semimetallicity of Co_2MnGa has been experimentally confirmed through photoemission spectroscopy [2], the giant anomalous Hall effect, and the giant Nernst effect [3].

The crystallinity of Heusler alloy is always an important issue [4–7]. The ideal crystal structure of Co_2YZ type full Heusler alloy is called $L2_1$, in which all atoms occupy regular sites. Atomic swaps between Co and Y, Co and Z, Y and Z, and among Co, Y and Z may occur, resulting in disordered structures. The Y–Z and Co–Y–Z-disordered structures are referred to as $B2$ and $A2$, respectively. Under non-stoichiometric conditions, excess antisite defects of particular elements may also be introduced depending on the details of the composition. One experimental study has suggested that the electrical transport properties are influenced by Co–Mn disorder or excess Co/Mn antisite defects [8]. Theoretical studies have suggested that the experimentally observed low half-metallicity and degraded electric performance may be explained by considering disorder and excess antisite defects [9–15].

Furthermore, the inclusion of a large amount of vacancies was also found experimentally [16], and the effects of

* Author to whom any correspondence should be addressed.

vacancies on the half-metallicity and electrical transport properties have been theoretically examined [12, 15, 17, 18]. The crystal disorder and point defects are almost unavoidable due to the difficulties in achieving ideal thermal equilibrium and stoichiometry, and the different vapor pressures of the constituents.

The effects of crystal disorder and defects on the Weyl transport properties of Co_2MnGa may also be of some importance considering the facts that (i) the Hall conductivity depends on the crystal quality, (ii) the sign of experimental transverse thermoelectric conductivity is not fully consistent with that expected from theoretical calculations assuming a perfect crystal, and (iii) the effects of stoichiometry and the resultant defect formation on doping state (electron/hole doping) have not been clarified [2, 3, 19–21].

Positron annihilation spectroscopy is an established and powerful method for detecting atomic vacancies in crystalline solids [22, 23]. The spin-polarized version, spin-polarized positron annihilation spectroscopy, enables the investigation of magnetism associated with bulk and atomic vacancies [24, 25]. In this study, we applied this technique to a conventionally produced Co_2MnGa bulk single crystal with a long range $L2_1$ order and high stoichiometry [26]. The results show that the Co_2MnGa crystal contains a high-density of single vacancies especially at Ga sites and that ferromagnetism is maintained in the vicinity of the vacancies.

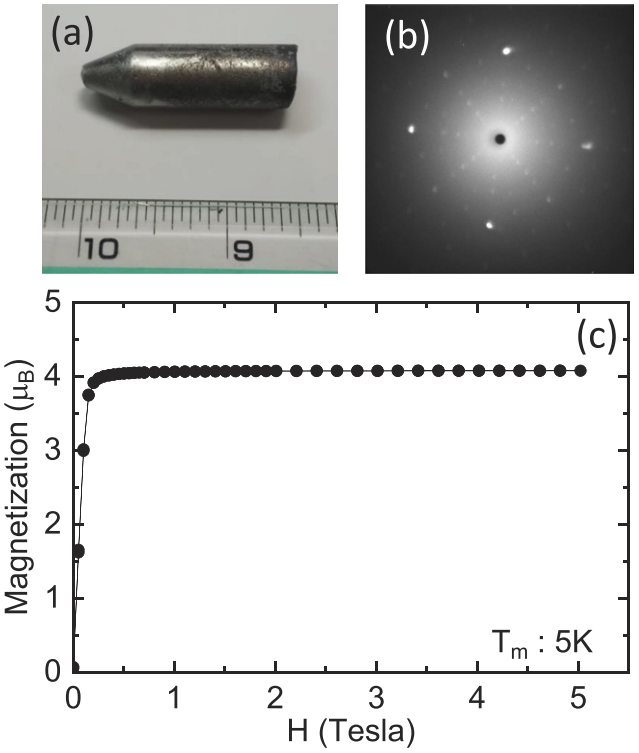

Figure 1. (a) Photo of the Co_2MnGa crystal grown in this work. (b) Back-reflected Laue pattern along the [100] direction. (c) Magnetization curve measured at 5 K.

2. Experimental

A Co_2MnGa bulk single crystal ($\phi 5 \times 15$ mm) was grown by the Bridgman method with a pulling rate of 10 mm h^{-1} at 1438 K from an ingot formed by conventional arc melting [27]. After growth, the crystal was kept at 1323 K for 20 days and at 873 K for 1 day for homogenization before being cooled to room temperature. The cooling rate was regulated to be 1 K min^{-1}. Disk samples (0.5 mm thick) with (001) surface orientation were cut out from the prepared single crystal. To remove the surface damage layer due to the cutting procedure and to obtain a smooth surface, the samples were mechanically polished with emery paper (#2000) and finished with 0.1 μm grade diamond paste. Figures 1(a) and (b) show the crystal ingot and the back-reflected Laue pattern along the [100] direction (RASCO-IIBLA, Rigaku; tungsten tube, 30 kV–30 mA). The $L2_1$ crystal ordering was also confirmed by powder neutron scattering measurements [28]. The alloy composition was determined to be Co:Mn:Ga = 50.3:24.9:24.8 by inductively coupled plasma mass spectrometry (IRIS Advantage DUO, Thermo Fisher Scientific Inc.). From the composition, the number of valence electrons was estimated to be $N_v = 28.1$, which is only slightly higher than that of the stoichiometric composition ($N_v = 28$). The present sample therefore corresponds to the weakly electron-doped condition. As shown in figure 1(c), the saturation magnetization was determined to be 4.07 $\pm$ 0.01 μ_B/f.u. at 5 K by superconducting quantum interference device measurement (MPMS-5S, Quantum Design). A Co_2MnAl polycrystal formed by arc melting followed by heat treatment at 1473 K for 20 h (purchased from Kojundo Chemical Laboratory Co., Ltd) was used as a reference. The composition was determined to be Co:Mn:Al = 49.7:25.2:25.1 by scanning electron microscopy with energy-dispersive x-ray analysis (SEM-EDX; SU3500/Horiba EX270, Hitachi). X-ray diffraction structural analysis (SmartLab diffractometer, Rigaku) found *B*2-ordered structure. The saturation magnetization was determined to be 3.75 $\pm$ 0.01 μ_B/f.u. at 300 K (MPMS, Quantum Design). The magnetization was slightly lower than the ideal value of 4 μ_B/f.u. because of the measurement temperature.

The samples were subjected to conventional positron lifetime measurement using a ^{22}NaCl source (200 kBq) deposited onto a 2 μm-thick Ti film. The spectrum data were analyzed by the PATFIT-88 program [29]. The time resolution was determined to be 240 ps full width at half-maximum (FWHM) of the Gaussian resolution function. In each spectrum, $\sim 10^6$ counts were accumulated. The lifetime spectra contained two instrumental components (typical lifetimes: 270 ps and 1.6 ns; intensities: 15% and 1.5%) related to the positron annihilation in the source and in the sample-source space, respectively. After subtracting these components, the lifetime spectra were fitted to exponential decay components. The samples were also examined by coincidence mode Doppler broadening of annihilation radiation (DBAR) measurement using a ^{22}NaCl source (78 MBq) deposited onto a carbon tray capped with a 5 μm-thick Ti window in an out-of-plane magnetic field of 1 T. The energy resolution was 0.7 keV FWHM of the anti-diagonal spectrum in the two-dimensional DBAR map [30].

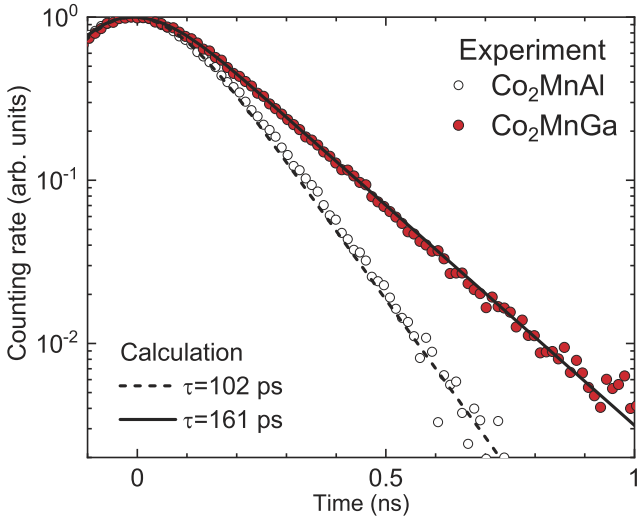

Figure 2. Positron lifetime spectra obtained for the Co_2MnAl (open circles) and the Co_2MnGa (filled circles) samples after source correction. Dashed and solid curves show simulated lifetime spectra with lifetimes of 102 ps (Co_2MnAl bulk) and 161 ps (Ga vacancy in Co_2MnGa), respectively.

In each spectrum, $\sim 3 \times 10^6$ counts were accumulated. The source-sample distance was 7 mm and the longitudinal spin polarization of positrons implanted into the sample was 40%. By changing the field direction between parallel and antiparallel relative to the polarization direction, we obtained the magnetic DBAR (MDB) spectrum $N_+(p) - N_-(p)$ as well as the total spectrum $(N_+(p) + N_-(p))$, where $+/-$ denotes the parallel/antiparallel field direction and p denotes the electron momentum [31, 32].

3. Theoretical calculations

To interpret the experimental data, density functional theory (DFT) calculations were conducted using the ABINIT code [33] with the projector augmented wave method [34] within the generalized gradient approximation [35]. The initial valence electron configurations were assumed to be $3s^2 3p^6 3d^8 4s^1$ (Co), $3s^2 3p^6 3d^6 4s^1$ (Mn), $3d^{10} 4s^2 4p^1$ (Ga) and $3s^2 3p^1$ (Al). For the calculation of the electronic states, a $2 \times 2 \times 2$ primitive cell with 32 atoms and a $2 \times 2 \times 2$ conventional cell with 128 atoms were constructed. The experimental lattice constants (5.77 Å for Co_2MnGa and 5.75 Å for Co_2MnAl) [4, 36] were used.

A self-consistent positron wave function without modifying the electronic states was obtained using two-component DFT in order to minimize the energy functional [37]. The core electron wave functions were represented by the Slater function parameterized by Clementi and Roetti [38], and the Borónski–Nieminen enhancement factor [37] was adopted. The DBAR spectra were obtained by convoluting the one-dimensional angular correlation of the annihilation radiation spectra obtained from the momentum density with the Gaussian resolution function having an FWHM of $2.74 \times 10^{-3} m_0 c$.

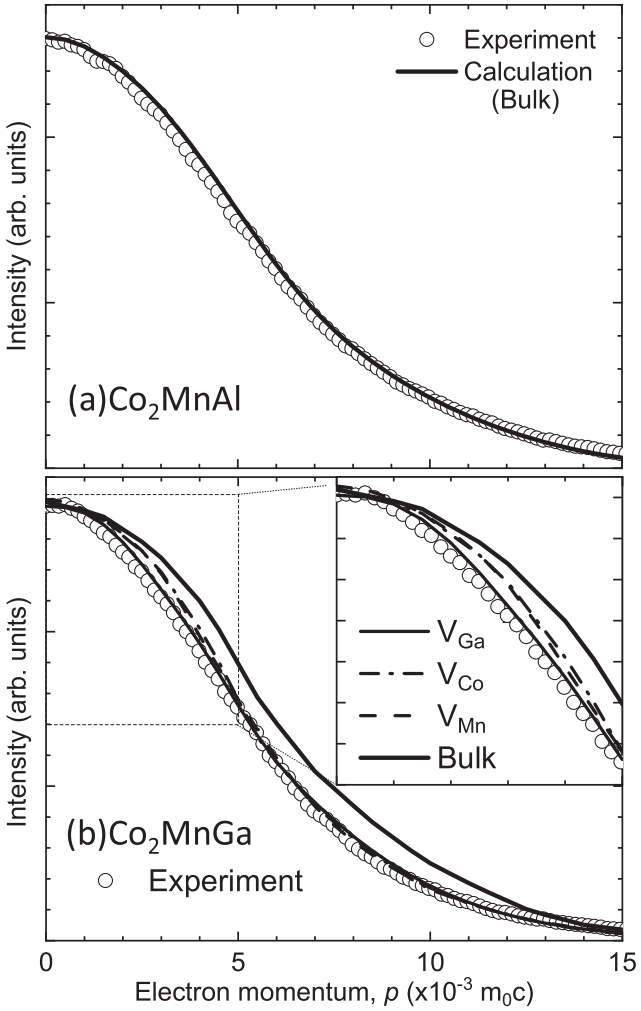

Figure 3. (a) DBAR spectrum obtained for the Co_2MnAl sample (open circles) and the calculated curve for the bulk (thick solid line). (b) DBAR spectrum obtained for the Co_2MnGa sample (open circles). Calculated curves for the bulk (thick solid curve), systems with a Co vacancy (dash-dotted curve), a Mn vacancy (dashed curve), and a Ga vacancy (thin solid curve) are also shown.

4. Results

4.1. Co_2MnAl sample

Figure 2 (open circles) shows the positron lifetime spectrum obtained for the Co_2MnAl sample. Only a single lifetime of 111 ± 4 ps was obtained. The dashed line shows the simulated spectrum using the calculated bulk lifetime of 102 ps. Although the experimental spectrum approximately agrees with the simulated one, a small discrepancy (9 ps) still remains. This may be ascribed to uncertainties in the evaluation of electron–positron correlation (many-body) effect, which generally occur in evaluation of the bulk lifetime. Thus, the obtained positron lifetime may be regarded as the bulk lifetime. Even if vacancies exist, the concentration is expected to be close to the detection limit ($0.1 \sim 1$ ppm).

Figure 3(a) shows the total DBAR spectrum $(N_+(p) + N_-(p))$ obtained for the Co_2MnAl sample (open circles) and

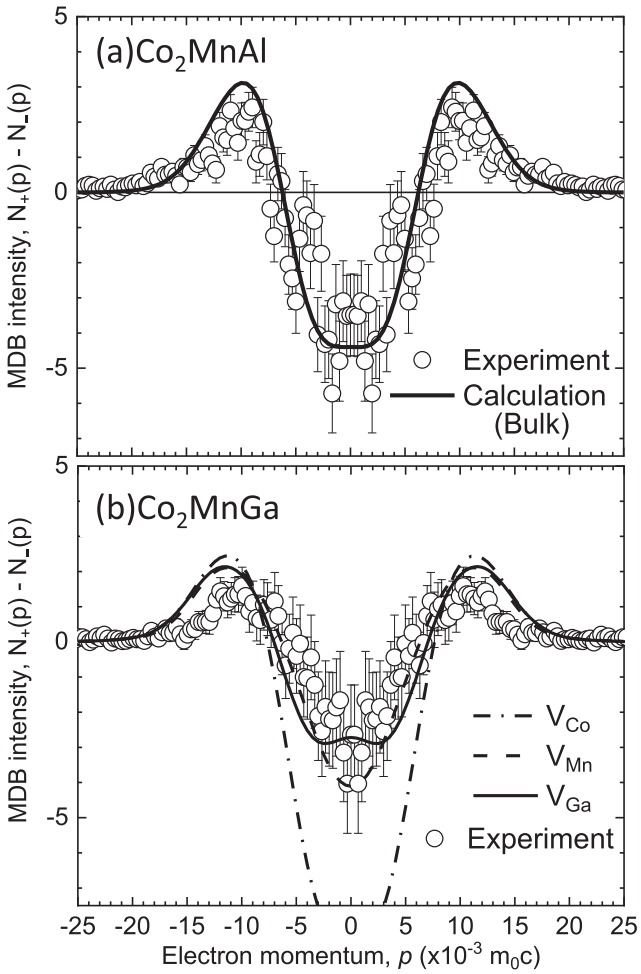

Figure 4. (a) MDB spectra obtained for the Co_2MnAl sample and calculated curve for the bulk (thick solid line). (b) MDB spectra obtained for the Co_2MnGa sample (open circles). Calculated curves are also shown for Co vacancy (dash-dotted curve), Mn vacancy (dashed curve), and Ga vacancy (solid curve) including an amplitude adjustment by 0.4. Experimental spectra of positive and negative momentum parts were folded for better statistics. The error bars are the statistical uncertainties depending on the event numbers.

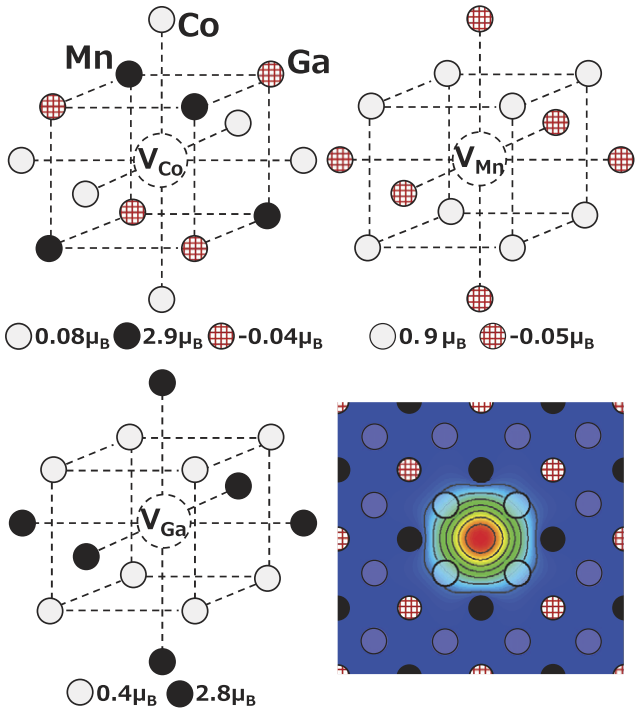

Figure 5. Schematic diagrams of Co, Mn, and Ga vacancies in Co_2MnGa. The calculated positron density map at Ga vacancy on the $(00\frac{1}{4})$ plane. Co atoms on the $(00\frac{1}{2})$ plane is also shown. The numbers are the calculated magnetic moments of individual atoms.

the calculated curve for the bulk (solid line). The experiment again agrees with the calculation for the bulk.

Figure 4(a) shows the MDB spectrum $(N_+(p) - N_-(p))$ for the Co_2MnAl sample and the calculated curve for the bulk after adjustment of the up-peak-to-down-peak amplitude by a factor of 0.4 which corresponds to the spin polarization of positrons. The experiment agrees with the calculation here, too.

Thus, there is no strong evidence for positron trapping at vacancies in the Co_2MnAl sample. That is, the vacancy concentration is under the detection limit (<0.1–1 ppm).

4.2. Co_2MnGa sample

Figure 2 (filled circles) shows the positron lifetime spectrum for the Co_2MnGa sample. Only a single lifetime of 161 ± 6 ps was obtained and further decomposition of the spectrum was difficult. The calculated bulk lifetime for Co_2MnGa was 100 ps. Obviously, the experimental positron lifetime is longer than the calculated bulk lifetime. This means that nearly all of the positrons are trapped at vacancies. The positron lifetimes for vacancies in Co_2MnGa were calculated to be 142 ps (Co vacancy), 154 ps (Mn vacancy), and 161 ps (Ga vacancy). The site-dependent positron lifetime simply reflects the effective electron density seen by positrons as shown in figure 5. Considering the local atomic arrangement around vacancies and the number of electrons for each element (15 [Mn], 17 [Co], and 20 [Ga] outside the Ar nucleus), the effective electron density at Ga vacancy, for instance, is the lowest among the three types of vacancies. As shown by the solid line in figure 2, the experimental positron lifetime spectrum is in excellent agreement with the simulated lifetime for Ga vacancies.

Figure 3(b) shows a comparison between the experimental DBAR spectrum for the Co_2MnGa sample and the theoretical curves. Again, the experiment is in good agreement with the calculated curves for vacancies, particularly for the Ga vacancy as shown in the inset.

Figure 4(b) shows the MDB spectrum $(N_+(p) - N_-(p))$ for the Co_2MnGa samples and the calculated curves for single vacancies. In the calculation, $\sim$90% of the positrons localized at single vacancies annihilated with electrons of the 1st nearest-neighbor (NN) atoms and the rest annihilated with electrons of the 2nd NN atoms. The magnetizations of individual atoms around vacancies were also calculated as shown in figure 5. Consequently, the effective magnetization around a vacancy as experienced by positrons varies from $\sim 10\ \mu_B$ for the Co vacancy and $\sim 6\ \mu_B$ for the Mn vacancy to $\sim 4\ \mu_B$ for the Ga vacancy. Hence, the MDB amplitude for Co vacancy (Ga vacancy) is the largest (smallest). The experiment agrees with

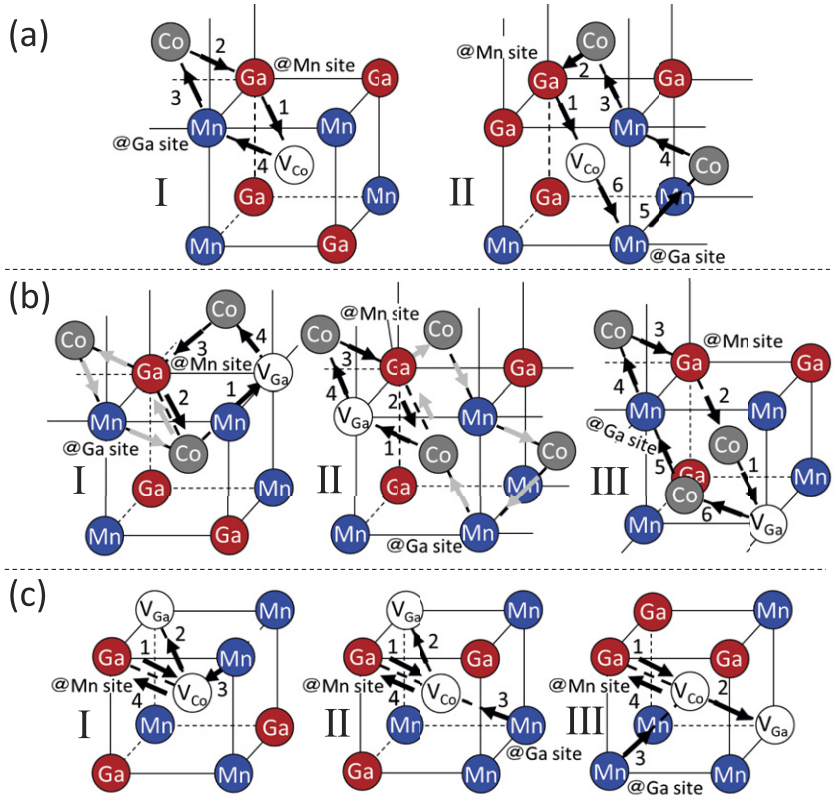

Figure 6. Schematic models of atomic exchange processes for Mn–Ga-disordered cells plus (a) one Co vacancy, (b) one Ga vacancy, and (c) one divacancy. These models are further classified into sub-models I to III. Black arrows indicate the initial elemental jumping processes that proceed in the order of the numbers beside the arrows. Gray arrows indicate a subsequent jumping process.

the calculations for Ga and Mn vacancies. Although a clear difference is not seen between Mn and Ga vacancies, this does not rule out the possibility that Ga vacancies are the main positron trapping centers. An important finding here is that the observed vacancies have magnetic moments.

The above results thus leave no doubt about the inclusion of Ga vacancies in the Co_2MnGa sample. Although other types of single vacancies may also be present, their concentrations are expected to be much lower than the concentration of Ga vacancies. Considering that nearly all positrons were trapped at Ga vacancies, the concentration is expected to be more than 100 ppm, which is the upper limit in the region where the positron trapping rate is proportional to the vacancy concentration. Overlap of positron wave functions between adjacent vacancies starts to become significant when the concentration of vacancies exceeds 1 $\sim$ 10 at.% to reduce the positron lifetime as known from a conventional calculation based on the atomic superposition method [39]. Hence, the vacancy concentration may be above 100 ppm and below the level of atomic %.

5. Discussion

5.1. Origin of excess vacancies in Co_2MnGa

According to theoretical studies [12, 15], the vacancy formation energies in Co_2YZ Heusler alloys (Y: Mn or Ti, Z: Si) are $\sim$1 eV (Co vacancy), 1–2 eV (Y vacancy), and 2–4 eV (Z vacancy). We confirmed similar tendencies for Co_2MnAl and Co_2MnGa through simpler calculations. Thus, thermally, Co vacancies are the most likely to form and Z vacancies are the least likely to form.

As shown in the preceding section, the vacancy concentration in the Co_2MnAl sample was under the detection limit ($<$0.1–1 ppm). This indicates that thermal vacancies that form at high temperatures disappear in the furnace-cooling process from 1473 K to room temperature. In other words, the furnace cooling is slow enough to allow vacancies to migrate to sinks.

In contrast, the Co_2MnGa sample was found to contain excess Ga vacancies. Considering the careful heat treatment for this sample as described in section 2, thermal vacancies are not expected to remain after the cooling process similar to the Co_2MnAl sample. It is thought that the Ga-poor condition ($\sim$0.2 at.% less than Co plus Mn) may be the reason for the excess Ga vacancies. In this context, the upper limit of the concentration of Ga vacancies may be $\sim$0.2 at.%, which is not inconsistent with the rough estimate from the positron lifetime data as mentioned above.

Thus, the observed excess Ga vacancies in the Co_2MnGa sample may be explained as structural vacancies. However, if vacancies are introduced simply due to off-stoichiometry, then, at most $\sim$0.3 at.% of Co vacancies may be expected for the Co_2MnAl sample because of the 0.3 at.% Co-poor condition of the sample. But, the actual concentration of vacancies was far below this. This implies that there are other reasons

for the extremely high concentration of vacancies introduced in Co_2MnGa other than off-stoichiometry.

It is known empirically that more vacancies are introduced in Co_2MnZ Heusler alloy by replacing Z element with greater atomic numbers (Z_A), e.g., $Z_A(Si) = 14 \rightarrow Z_A(Ge) = 32 \rightarrow Z_A(Sn) = 50$ [16], and the quite low and extremely high vacancy concentrations observed respectively for the Co_2MnAl ($Z_A = 13$) and Co_2MnGa ($Z_A = 31$) samples are in agreement with this. Because the theoretical formation energies of vacancies change only slightly depending on Z_A, this does not explain the above empirical law. There is expected to be some other reasons for the change in vacancy concentration depending on Z_A. Further studies especially based on theories are needed into the above question.

5.2. Role of vacancies in crystal ordering

The Co_2MnAl sample with Mn–Al-disordered $B2$ structure was nearly vacancy-free, while the Co_2MnGa sample with highly ordered $L2_1$ structure was vacancy-rich. This fact implies the possibility that vacancies facilitate the development of highly ordered $L2_1$ structure through vacancy-assisted atomic diffusion.

Although Co thermal vacancies may be the majority vacancies at high temperatures because of the relatively low formation energy, the Co_2MnGa sample contains a large amount of Ga vacancies in addition to Co thermal vacancies. Hence, Ga vacancies may be essential in the transformation from the Mn–Ga-disordered $B2$ structure to the highly ordered $L2_1$ structure. To investigate this, we carried out model calculations assuming Mn–Ga-disordered cells with a Co vacancy (Co-vacancy-mediated model) [40], a Ga vacancy (Ga-vacancy-mediated model), or a NN Co–Ga divacancy (divacancy-mediated model).

Figure 6(a) shows two configurations of the Co-vacancy-mediated model. One (I) includes a Mn antisite, a Ga antisite, a Co atom, and a Co vacancy in a diamond loop. Atomic exchange proceeds among them to cancel the Mn and Ga antisites. The other (II) has a diagonally aligned Mn antisite, Co vacancy, and Ga antisite. Atomic exchange to cancel the Mn and Ga antisites may be possible for instance by the loop shown in the figure. Similarly, figure 6(b) shows three configurations of the Ga-vacancy-mediated model. In I and II, the Ga antisites first move to the regular Ga sites (initially Ga vacancies) according to the diamond loops of black arrows, and then the Mn antisites move to the regular Mn sites according to the loops of gray arrows. In III, atomic exchange is assumed to occur in a larger loop as shown in the figure. Figure 6(c) shows three configurations of the divacancy-mediated model. First, the Ga antisites move to the regular Ga sites through the divacancies and then the Mn antisites similarly move to the regular sites. Thus, for individual cases of (a) to (c), several patterns were examined.

Figures 7(a)–(c) show the calculated energy curves for the three models in figures 6(a)–(c). Each step was divided into four segments, i.e., the paths from 0–1/4, 1/4–1/2, 1/2–3/4 to 3/4–1 and the differences of total energies from the initial one were plotted. In the Co-vacancy-mediated model (figure 7(a)),

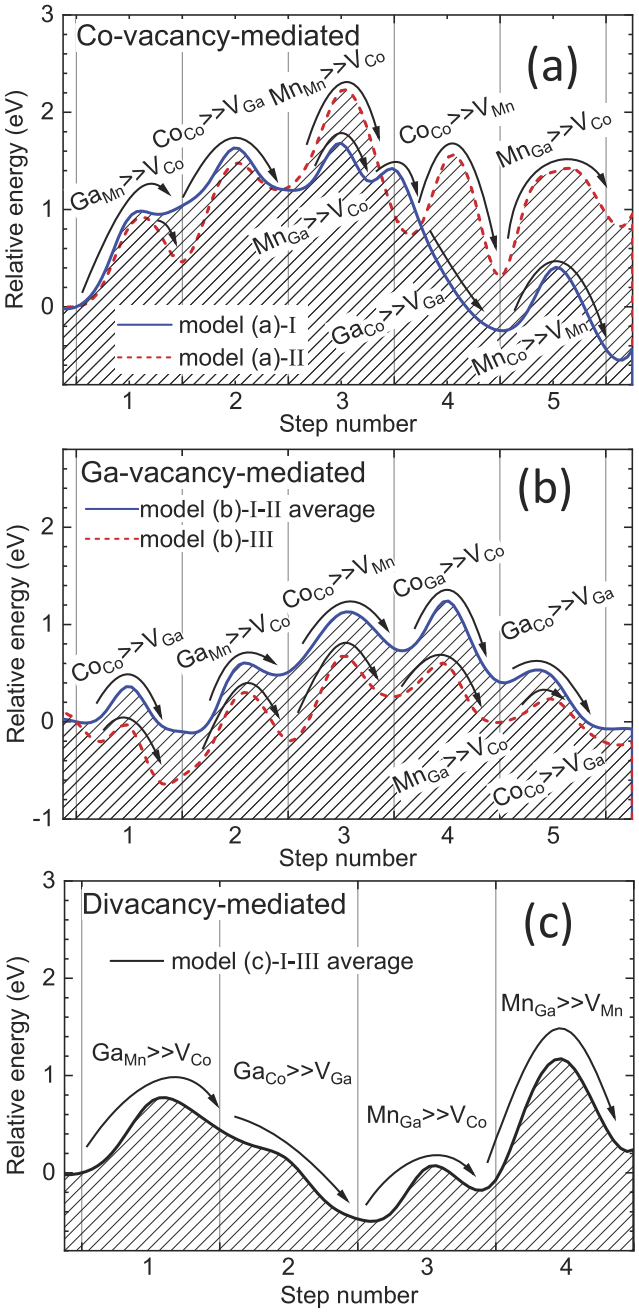

Figure 7. Calculated energy curves for the (a) Co-vacancy-mediated model, (b) Ga-vacancy-mediated model, and (c) divacancy-mediated model shown in figure 6. In model (b), sub-models I and II are averaged. In model (c), sub-models I to III are all averaged.

the highest energy barrier among all the steps shown here is approximately 1 eV. Except for step 1 of configuration (a)-I, all the other steps exhibit well-formed saddle points. Therefore, the Co-vacancy-mediated atomic diffusion basically easily occurs at high temperatures, e.g., above 1000 K. Consequently, the original Ga antisite is finally canceled ($Ga_{Co} \rightarrow V_{Ga}$). In the Ga-vacancy-mediated model (figure 7(b)), the individual energy barriers are again less than 1 eV, but the overall energy barrier measured from the initial energy, i.e., ∼1.2 eV at the middle of step 4, is lower than that in the Co-vacancy-mediated model (∼2.2 eV at the middle of

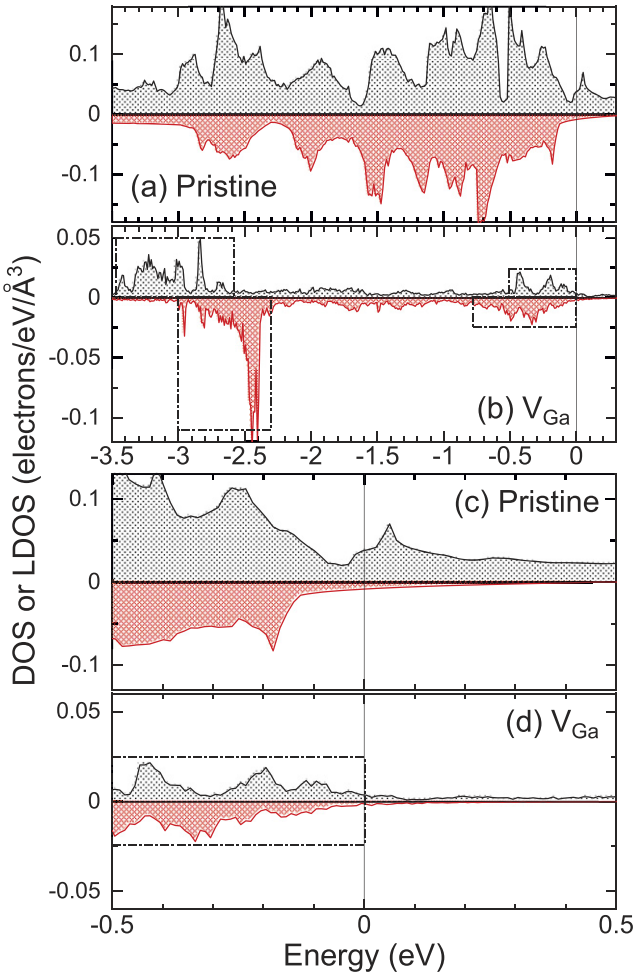

Figure 8. (a) and (c) Calculated DOS for pristine Co_2MnGa. (b) and (d) Calculated LDOS in a sphere with the radius of 1 Å at Ga vacancy. The positive and negative DOSs represent the majority and minority spin channels. The Fermi level is at 0 eV. The areas surrounded by the dash-dotted boxes highlight the states related to the Ga vacancy.

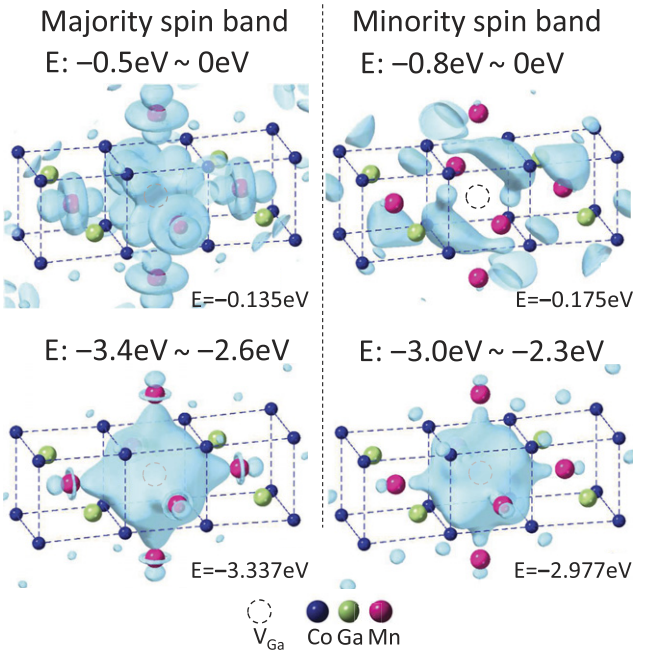

Figure 9. Examples of electron wave functions around the Ga vacancy at the Γ point obtained from the dispersions that are different from the bulk-like dispersions.

step 3). This suggests that the Ga-vacancy-mediated atomic diffusion occurs more easily than the Co-vacancy-mediated case. In the divacancy-mediated model, the Ga atoms also easily move to the regular Ga sites ($Ga_{Mn} \rightarrow V_{Ga}$) with the low energy barrier of ∼0.6 eV, and hence the original Ga antisite is immediately canceled. The energy barriers for the movement of Mn atoms to the regular Mn sites ($Mn_{Ga} \rightarrow V_{Mn}$) is also only ∼1 eV. Thus, the above calculation indicates that Ga vacancies may play an important role in facilitating the atomic exchange processes for developing the $L2_1$-ordered structure.

5.3. Electronic states associated with vacancies

Figures 8(a) and (c) show the calculated density of states (DOS) for pristine Co_2MnGa. (To avoid artificial structures as much as possible, the calculation was carried out using a k-point grid of 24 × 24 × 24.) Above the Fermi level, the majority spin band has relatively low states and large dispersions (figure 8(c)). This shows the effect of *sd*-hybridization. The peak at ∼50 meV above the Fermi level is due to the flat dispersion around the bottom of the *sd*-hybridized bands. The smaller number of states above the Fermi level in the minority spin band gives rise to the pseudo-gap and hence the half-metallicity. Below the Fermi level, the contribution from *d* bands starts to become predominant (figure 8(a)) in both the majority and minority spin bands.

Figures 8(b) and (d) show the local DOS (LDOS) in a sphere with the radius of 1 Å at Ga vacancy. Contrarily to the pristine system, two specific energy regions appear as highlighted by the dash-dotted boxes in the figure. That is, E: −0.5 eV to 0 eV and E: −3.4 eV to −2.6 eV for the majority spin band, and E: −0.8 eV to 0 eV and E: −3.0 eV to −2.3 eV for the minority spin band. We found that these shallow and deep states below the Fermi level have dispersions distinguished from those for the pristine system. Hence, these states may be associated with Ga vacancy. We also found that new states associated with Co and Mn vacancies (results not shown) appear in the pseudo-gap of the minority spin band as already predicted for other Co_2MnZ Heusler alloys [12, 15, 17, 18]. From this, the difference of Ga vacancy from Co and Mn vacancies were confirmed.

Figure 9 shows examples of the electron wave functions of the above-mentioned shallow and deep states at the Γ point. The wave functions for $E = -3.337$ eV and −2.977 eV are strongly localized at the Ga vacancy. Hence, these deep states are undoubtedly identified as vacancy-related. As exemplified by the wave function at $E = -0.135$ eV in the majority spin band, the shallow states in this channel are mainly composed of 2nd NN Mn *d*-electrons. Similarly, from the wave function at $E = -0.175$ eV in the minority spin band, the shallow states in this channel are mainly composed of 1st NN Co electrons. The

wave functions of the shallow states extend from the vacant sites to the outside. Since the shallow states exist just below the Fermi level, they may affect the electrical transport properties through the extrinsic scattering regime. Considering the fact that Ga vacancies have excess spins as confirmed both from the experiment and calculation, it is important to explore magnetic scattering of carriers through the calculation of the Berry curvature in future.

6. Conclusion

We investigated a single-crystalline Co_2MnGa with $L2_1$ structure and a polycrystalline Co_2MnAl with $B2$ structure using spin-polarized positron annihilation spectroscopy. In the Co_2MnAl polycrystal, the vacancy concentration was below the detection limit (<1 ppm). In contrast, a large amount of magnetic Ga vacancies (at least more than 100 ppm to at most the level of atomic %) was found to be introduced in the Co_2MnGa crystal. The off-stoichiometry was assumed to be one reason for this observation. However, the sharp difference between Co_2MnGa and Co_2MnAl could not be fully explained by off-stoichiometry alone. Calculations found that Ga vacancies have an important role in the development of $L2_1$-ordered structure. Spin-polarized electronic states related to Ga vacancies were also found to appear near the Fermi level. In these respects, the reasons for the inclusion of high-density vacancies should be explored continuously and thoroughly hereafter. Since Co_2MnGa is paid attention as the Weyl semimetal in the development of next-generation devices, the influence of high-density magnetic vacancies on the electrical performance is an important issue to be clarified.

Although much larger topological Weyl property is predicted for Co_2MnAl as compared to Co_2MnGa, it has not yet been confirmed experimentally. One reason is the difficulty in obtaining highly-ordered $L2_1$ structure. The present work implies that it is due to the lack of vacancies. If the highly-ordered $L2_1$ structure and the reduction of vacancies are hardly achieved simultaneously in principle, some effective options should be explored in the synthesis of Co_2Mn-based Weyl semimetals. The inclusion of atomic vacancies is also an important issue in other Weyl semimetals based on binary intermetallic compounds as well as the Heusler alloys. Again, toward the realization of new functional devices based on the Weyl semimetals, the issues of lattice defects should be investigated more exhaustively.

Data availability statement

All data that support the findings of this study are included within the article (and any supplementary files).

ORCID iDs

A Miyashita https://orcid.org/0000-0002-2829-1941
M Maekawa https://orcid.org/0000-0001-9172-1206
Y Shimoyama https://orcid.org/0000-0001-8007-4752
N Seko https://orcid.org/0000-0002-5600-7311
A Kawasuso https://orcid.org/0000-0002-7065-5753
R Y Umetsu https://orcid.org/0000-0003-0128-073X

References

[1] Kübler J and Felser C 2016 *Europhys. Lett.* **114** 47005
[2] Belopolski I *et al* 2019 *Science* **365** 1278
[3] Sakai A *et al* 2018 *Nat. Phys.* **14** 1119
[4] Webster P J 1971 *J. Phys. Chem. Solids* **32** 1221
[5] Graf T, Felser C and Parkin S S P 2011 *Prog. Solid State Chem.* **39** 1
[6] Galanakis I 2016 *Heusler Alloys, Properties, Growth, Applications* ed C Felser and A Hirohata (Berlin: Springer) p 3
[7] Wurmehl S and Wójcik M 2016 *Heusler Alloys, Properties, Growth, Applications* ed C Felser and A Hirohata (Berlin: Springer) p 87
[8] Raphael M P *et al* 2002 *Phys. Rev.* B **66** 104429
[9] Picozzi S, Continenza A and Freeman A J 2004 *Phys. Rev.* B **69** 094423
[10] Picozzi S and Freeman A J 2004 *J. Phys.: Condens. Matter.* **19** 315215
[11] Kota Y, Tsuchida H and Sakuma A 2009 *J. Phys.: Conf. Ser.* **200** 052012
[12] Hülsen B, Scheffler M and Kratzer P 2009 *Phys. Rev.* B **79** 094407
[13] Kudrnovský J, Drchal V and Turek I 2013 *Phys. Rev.* B **88** 014422
[14] Pradines B, Arras R, Abdallah I, Biziere N and Calmels L 2017 *Phys. Rev.* B **95** 094425
[15] Popescu V, Kratzer P, Wimmer S and Ebert H 2017 *Phys. Rev.* B **96** 054443
[16] Kogachi M, Kikuchi S, Fujiwara T and Hori F 2009 *J. Alloys Compd.* **480** 462
[17] Özdŏgan K, Sasioglu E and Galanakis I 2007 *Phys. Status Solidi (PRL)* **1** 184
[18] Pradines B, Arras R and Calmels L 2016 *J. Phys.: Conf. Ser.* **903** 012030
[19] Guin S N *et al* 2019 *NPG Asia Mater.* **11** 16
[20] Sumida K *et al* 2020 *Commun. Mater.* **1** 89
[21] Wang Q, Wen Z, Kubota T, Seki T and Takanashi K 2019 *Appl. Phys. Lett.* **115** 252401
[22] Krause-Rehberg R and Leipner H S 1998 *Positron Annihilation in Semiconductors* (Berlin: Springer)
[23] Tuomisto F and Makkonen I 2013 *Rev. Mod. Phys.* **85** 1583
[24] Li H, Maekawa M, Miyashita A and Kawasuso A 2017 *Defect Diffusion Forum* **373** 65
[25] Maekawa M, Miyashita A, Sakai S and Kawasuso A 2020 *Phys. Rev.* B **102** 054427
[26] Kono T, Kakoki M, Yoshikawa T, Wang X, Goto K, Muro T, Umetsu R Y and Kimura A 2020 *Phys. Rev. Lett.* **125** 216403
[27] Manna K *et al* 2018 *Phys. Rev.* X **8** 041045
[28] Umetsu R Y, Kobayashi K, Kainuma R, Yamaguchi Y, Ohoyama K, Sakuma A and Ishida K 2010 *J. Alloys Compd.* **499** 1
[29] Kirkegaard P, Pederson P and Erdlup M M 1988 PATFIT-88: a data-processing system for positron annihilation spectra on mainframe and personal computers *Risø-M No. 2740* Risø National Laboratory
[30] Kruseman A C, Schut H, van Veen A, Mijnarends P E, Clement M and de Nijs J M M 1997 *Appl. Surf. Sci.* **116** 192
[31] Kawasuso A, Maekawa M, Fukaya Y, Yabuuchi A and Mochizuki I 2011 *Phys. Rev.* B **83** 100406(R)
[32] Kawasuso A, Maekawa M, Fukaya Y, Yabuuchi A and Mochizuki I 2012 *Phys. Rev.* B **85** 024417

[33] Gonze X *et al* 2002 *Comput. Mater. Sci.* **25** 478
[34] Blöchl P E 1994 *Phys. Rev.* B **50** 17953
[35] Perdew J P, Burke K and Ernzerhof M 1996 *Phys. Rev. Lett.* **77** 3865
[36] Umetsu R Y, Kobayashi K, Fujita A, Kainuma R and Ishida K 2008 *J. Appl. Phys.* **103** 07D718
[37] Boroński E and Nieminen R M 1986 *Phys. Rev.* B **34** 3820
[38] Clementi E and Roetti C 1974 *At. Data Nucl. Data Tables* **14** 177
[39] Puska M J and Nieminen R M 1994 *Rev. Mod. Phys.* **66** 841
[40] Erdélyi G, Mehrer H, Imre A W, Lograsso T A and Schlagel D L 2007 *Intermetallics* **15** 1078